Simulation of Nanoparticle Permeation through a Lipid Membrane

Steven L. Fiedler and Angela Violi*
Department of Mechanical Engineering, University of Michigan, Ann Arbor, Michigan

ABSTRACT A metric of nanoparticle toxicity is the passive permeability rate through cellular membranes. To assess the influence of nanoparticle morphology on this process, the permeability of buckyball-sized molecules through a representative lipid bilayer was investigated by molecular-dynamics simulation. When C_{60} was compared with a prototypical opened C_{60} molecule and a representative combustion-generated particle, $C_{68}H_{29}$, the calculated free-energy profiles along the permeation coordinate revealed a sizable variation in form and depth. The orientation of the anisotropic molecules was determined by monitoring the principal axis corresponding to the largest moment of inertia, and free rotation was shown to be hindered in the bilayer interior. Diffusion constant values of the permeant molecules were calculated from a statistical average of seven to 10 trajectories at five locations along the permeation coordinate. A relatively minor variation of the values was observed in the bilayer interior; however, local resistance values spanned up to 24 orders of magnitude from the water layer to the bilayer center, due primarily to its exponential dependence on free energy. The permeability coefficient values calculated for the three similarly sized but structurally distinct nanoparticles showed a significant variance. The use of C_{60} to represent similarly sized carbonaceous nanoparticles for assessments of toxicity is questioned.

INTRODUCTION

It is known that particle toxicity can scale inversely with size (1). Although the relative detrimental health effects of micrometer-sized particles have received significant attention over the past century, less is known about the potential toxicity of ultrafine particles ($\leq$100 nm). Since nanometer-sized particles (NPs) that are capable of crossing cellular barriers can migrate into systemic circulation, attention is given to factors that influence the permeation process. Additionally, the presence of trapped, hydrophobic NPs can instigate changes in lipid packing and influence the phase behavior of the bilayer (2,3). Reciprocally, the permeability of molecular NPs into lipid bilayers is regulated by the fluidity and composition of the bilayers themselves, as well as the morphology and polarity of the permeant molecules (4,5). It is currently hypothesized that small molecules (molecular mass $<$ 100 amu) hop from dynamic stochastic voids within the bilayer (4). The permeation of NPs larger than the free volumes would be expected to proceed by a different mechanism (6). A clear difference in the permeation of small molecules vis-à-vis NPs has been shown by computational simulation and calculation of the so-called local diffusion constant as a function of permeant depth, z, within the bilayer. Variability of the diffusion constant values of the small molecular permeants with respect to z has been asserted to correlate to membrane heterogeneity, i.e., differences in free volume as a function of permeant position along the bilayer norm. NP diffusion constant values, however, have been observed to be relatively independent of molecular position in bilayer interior (6).

One defined property of both the small molecule and NP permeation process is the tendency of anisotropic molecules to preferentially orient with the major axis aligned parallel to the bilayer norm. This alignment has been observed by NMR (7), fluorescence depolarization (8,9), x-ray diffraction (10), and second harmonic spectroscopic measurements (11), and matched by analysis of molecular-dynamics (MD) simulations (6,12). According to the free-volume model (13), the cross-sectional area of the permeant could then be a key parameter in the diffusion process, since the permeant advancement would be based on encounters with voids exceeding the areal dimensions. Assessment of the alignment also provides a connection to a thermodynamic description of the permeation process (12,14). Conventionally, the translocation of hydrophobic particles into lipid bilayers has been attributed to an overall entropically driven process (15,16), considered to be a consequence of the hydrophobic effect. The size of the permeant molecule, however, has also been shown to influence the physics of aqueous solvation. Simulations have demonstrated that larger solutes are capable of disrupting water hydrogen bonds in the first solvation shell (17). This in turn, can alter the contribution of enthalpy versus entropy to the free energy of permeation or solvation. In a more general sense, evaluation of the total free energy can be used to determine the probability of the permeation process (18) (i.e., the lipophilicity of the permeant), quantitatively map entry barriers (15,19), indicate equilibrated locations of the permeants in the membrane (15), and obtain temporal estimates for membrane/permenat dynamics (14). Partition coefficient values can also be determined by assessing free-energy differences within the rubric of the inhomogeneous solubility-diffusion model (20). As such, the influence of the lipid bilayer microstructure is directly reflected. Similarly,

Submitted February 3, 2010, and accepted for publication March 10, 2010.

*Correspondence: avioli@umich.edu

Editor: Gregory A. Voth.

© 2010 by the Biophysical Society

0006-3495/10/07/0144/9 $2.00

doi: 10.1016/j.bpj.2010.03.039

the diffusion constant values of permeants within the bilayer can be extracted from MD simulations based on an autocorrelation of temporal fluctuations of the net force acting on the permeant (20–22). In this manner, approximations inherent to the Einstein and Green-Kubo (23) relations in this environment can be circumvented (24). Permeability coefficient values that are sensitive to the membrane heterogeneity can be thus be obtained as an integrated product of local diffusion and partition coefficients (25).

The objective of this study was to determine the interaction of nonpolar, carbonaceous NPs with lipid bilayers. The passive permeability coefficient value of the buckyball molecule has been calculated to be exceptionally high, surpassing that of the aforementioned smaller molecules by an order of magnitude (26). In this context, we also considered the permeation of a C_{60}-sized, combustion-generated, pollutant-type particle, due to the enhanced probability of environmental exposure. An intermediate particle served to assist assessment of the relevant contributions to the permeation process. To achieve adequate statistics required for the diffusion constant calculations (6), we carried out a series of multiple MD simulations. Concurrently, what we believe to be a novel approach was developed and applied to assess the orientation of the anisotropic molecules, which afforded an assessment of the orientation oscillations, i.e., a determination of the degree to which the orientation of a permeant was locked in place.

MATERIALS AND METHODS

Configuration constructs and parameterization

Three nanoparticles were included in this study: 1), buckminsterfullerene C_{60}; 2), a representative combustion-generated NP termed NanoC (Fig. 1 *a*); and 3), an open C_{60} fullerene termed Open-C_{60} (Fig. 1 *b*). Coordinates for C_{60} were obtained from the default coordinates of Gaussview 3 (27). The Atomistic Model Particle Inception (AMPI) program (28) was employed to generate NanoC ($C_{68}H_{29}$). AMPI, which is based on the principle of combining kinetic Monte Carlo and MD techniques to bridge timescales between and during reaction events, has been shown to be a computationally tractable approach for calculating NP structures of up to hundreds of atoms generated in a flame environment (29–31). After the particles were formed, radical sites were terminated with hydrogen atoms. Each calculated umbrella-shaped particles had nearly equal dimensions of length and width (1.07 nm ×1.1 nm, respectively). The Open-C_{60} molecule was created by artificially paring down a C_{100} fullerene with a pentagonal and hexagonal face (32) to a 60 carbon atom structure.

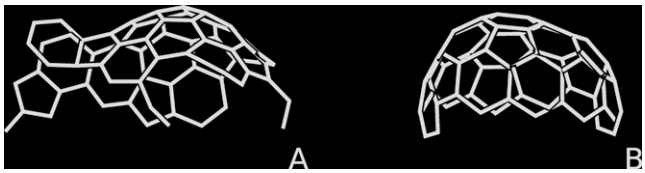


FIGURE 1 (*A*) NanoC: structure of a nanosized organic particle from a propane flame environment. (*B*) Open-C_{60}: a prototypical open-shell fullerene.

For MD simulation, the DL_POLY 2.17 GUI (33) was used to generate nanoparticle intramolecular forces. As an improvement over previous studies (5,34) angular constraints were not imposed, which allowed the particle to possess a more realistic, flexible structure. The representative membrane was comprised of a 3:1, mixed-phase, dimyristoylphosphatidylcholine (DMPC), cholesterol bilayer. The DMPC and cholesterol force fields were taken from the United Atom Optimized Potentials for Liquid Simulations (UA-OPLS)-based parameterization of Smondyrev and Berkowitz (35,36), and permeant nonbonded potential parameters were similarly assigned UA-OPLS values for consistency. Water molecules were specified by the TIP3P parameterization (36), and all lipid and water bonds were constrained with the SHAKE algorithm. Force-field parameters were converted to GROMACS format and validated by comparison of individual energetic contributions to ensure a proper porting. Except when otherwise noted, equations of motion were integrated using GROMACS simulation package versions 3.3.1 and 4.0.5 in single precision (37).

The initial bilayer system configuration consisted of a 3.26 × 4.37 × 7.27 nm^3 box containing 48 DMPC molecules interspersed with 16 cholesterol molecules and solvated above and below with 1372 H_2O molecules. The bilayer norm was defined to be parallel with the *z*-coordinate axis, with distance *z* originating from the bilayer center and extending 3.4 nm into the aqueous phase. Periodic boundaries conditions were used in all directions. van der Waals and Coulomb cut-offs were set to 1.5 nm, and the particle mesh Ewald summation was used for electrostatic interactions with the default associated parameters. Simulations were performed in the isothermal-isobaric ensemble at a temperature of 308 K and a pressure of 1 atm maintained by a Berendsen thermostat (38) ($\tau = 0.1$ ps) and Parrinello-Rahman barostat (39) ($\tau = 1$ ps), respectively. Pressure coupling was applied isotropically to match the parameterization conditions (36). The sensitivity of the barostat scaling approach was tested by additionally considering decoupled (semiisotropic) expansion in the *xy*-plane from that along the *z*-coordinate axis, designed for interface systems.

Potential of mean force calculations

To calculate the free-energy values and diffusivity, the nanoparticles were inserted in 0.1 nm increments along the bilayer norm, resulting in 35 separate positions for each nanoparticle. To avoid local hysteresis, permeant molecules were reduced to 1/10th of their original size before insertion at a given location, the system was minimized to eliminate bad contacts and then equilibrated, and the intramolecular bonds of the scaled particle were then lengthened by a given fraction. The process then was repeated. It was found that 10 growth iterations were sufficient (e.g., when the resonant carbon bonds were increased from 0.14 Å to 1.4 Å). Calculations of the free-energy profiles as a function of position along the bilayer norm were carried out using the constraint force (CF) approach, as implemented in the GROMACS pull code with positions of the particles constrained to the *xy*-plane. It was determined that convergence of the potential of mean force calculations required simulation times of more than tens of nanoseconds. The systems were equilibrated for at least 4 ns, during which time the average normal forces showed significant fluctuation, and data were subsequently collected for the remaining 26 ns. The mean force uncertainties were calculated by the correlation analysis method (40) and propagated from the water phase toward the bilayer center for the integrated free-energy values. The depths of the free-energy binding of particles in the bilayer center were also calculated by the thermodynamic integration (TI) method using the GROMACS free-energy code. To this end, free-energy differences were evaluated by applying the relevant thermodynamic cycle and scaling the particles' nonbonding interactions with the environment. A set of 11 coupling parameter (λ) values, {0, 0.05, 0.1, 0.2, 0.3, …, 1.0} were used with a soft core σ-value of 0.3, scaling value of 0.5, and power value of 1.0, for the particles constrained inside and outside the bilayer at $z =$ 0 nm and 3.4 nm, respectively. Trajectories for the TI calculations were run for 8 ns.

Diffusion, resistance, and permeability constant calculations

For a given permeant, the normal diffusion constant values, $D(z)$, were calculated as a function of the autocorrelation function of the instantaneous force, $F(z,t)$, acting on the permeant molecule constrained to a given plane at a distance, z, above the bilayer center:

$$D(z) = \frac{(RT)^2}{\int_0^\infty \langle \Delta F(z,t) \cdot \Delta F(z,0) \rangle dt}, \quad (1)$$

where $\Delta F(z,t)$ is the difference between the instantaneous force and mean force $\langle F(z) \rangle$ acting on the permeant. To increase the sampling in this study, multiple independent trajectories (7–10) were averaged at each of five selected locations: the bilayer center ($z = 0$ nm), tail group region ($z = 0.9$ nm), headgroup region ($z = 1.7$ nm), interface boundary ($z = 2.5$ nm), and water layer ($z = 3.3$ nm). The initial configurations of each system were constructed using the particle growth approach as described above. Due to the large NP size, only one particle was inserted per configuration for planar distances of $z = 0.9$, 1.7, and 2.5 nm to avoid particle-particle interactions. To enhance computational efficiency, two particles were inserted per configuration for positions set in the bilayer center and water layer. Configurations were briefly equilibrated and run for 8 ns with atomic forces printed every 50 fs. The print frequency was determined by minimizing the autocorrelation calculation time while retaining the accuracy of the simulation. To validate the latter, the integrated force autocorrelation function (FAC) profiles were compared with profiles based on force values printed at every 2 fs step. The FAC values were calculated using in-house code written in the C programming language on a Unix/Linux platform using multiple time origins and unbiased averaging, and validated to values obtained by the Mathematica and MATLAB programs (The MathWorks, Natick, MA). For a given particle and planar position, the FAC profiles from the corresponding seven to 10 trajectories were averaged and fit to the standard double exponential decay (19). The integral of the fit was then applied in Eq. 1 to yield the respective diffusion constant value at the given planar level. To extract an estimate of the associated uncertainty, the individual FAC profiles were fit and a standard deviation was calculated from the resultant diffusion constant values from each trajectory. Together, the production runs of the free-energy and diffusion calculations required an aggregate of 5 μs of simulation time.

The permeation resistance $R(z)$ and subsequently the permeability coefficient, P, were calculated by the inhomogeneous solubility-diffusion approach (20), with the resistance expressed as

$$R(z) = \frac{\exp(\Delta G(z)/RT)}{D(z)}, \quad (2)$$

and integrated to yield the permeability coefficient,

$$P = \frac{1}{\int_{z>d/2}^{0} R(z)dz}, \quad (3)$$

for a bilayer of thickness, d. To determine the local resistance values, $R(z)$, the averaged diffusion constant values at $z = 0.0$, 0.9, 1.7, 2.5, and 3.3 nm for each molecule were interpolated using an Akima spline within the plotting software Grace, version 5.1.20 (41).

Molecular orientation

As part of our systematic approach to extract permeant orientations from the simulations independently of the number or orientation of hydrogen bonds, we sought to determine the appropriate principal axis of inertia of the permeant. To this end, permeant coordinates were parsed from the trajectory file at regular increments (50 fs), and the permeant moment of inertia tensor, $\tilde{I}$, was constructed:

$$\tilde{I} = \begin{bmatrix} I_{xx} & I_{xy} & I_{xz} \\ I_{yx} & I_{yy} & I_{yz} \\ I_{zx} & I_{zy} & I_{zz} \end{bmatrix} \quad (4)$$

with diagonal (I_{ii}) and off-diagonal (I_{ij}) matrix elements calculated as

$$I_{ii} = \sum_\alpha m_\alpha \left(q_{j\neq i}^2 + q_{k\neq i}^2 \right) \quad (5)$$

and,

$$I_{ij} = -\sum_\alpha m_\alpha q_i q_j \quad (6)$$

where m_α is the atomic mass of atom α, and q_{ij} is the respective atomic degree of freedom (42). Diagonalization of $\tilde{I}$ yields the permeant principal moments of inertia as the eigenvalues, and the respective principal axes are defined as the eigenvectors. By selecting the principal axis corresponding to the largest moment of inertia, one can determine the angle of orientation of the permeant with respect to the bilayer norm as the arcsine of the dot product of the principal axis and the unit vector of the norm, {0,0,1}.

RESULTS AND DISCUSSION

Free-energy profile

To provide a point of reference for the permeation of nano-sized molecules, we calculated the energy- and diffusivity-related values of a regular C_{60} buckminsterfullerene from simulation. The obtained free-energy profile of C_{60} permeating a DMPC/cholesterol bilayer (Fig. 2) is quantitatively similar in form to that previously observed by Bedrov et al. (26) in a neat DMPC bilayer. Given the differences in force-field parameterization between our study and the previous one, the agreement of prominent features in the profile lends confidence to the assignation of molecular behavior at given points, z, along the bilayer norm. In both studies, a lack of barrier was evident for the transition of C_{60} from the aqueous phase to the lipid headgroup region; furthermore, unconstrained MD simulations have revealed the spontaneous insertion of this permeant on the nanosecond time frame (26,43,44). The free-energy plateau, evident at 2.3–2.8 nm from the bilayer center, corresponds to the interface region (35,45,46). We attribute the constant free energy of the permeant traversing this region to a relative homogeneity of the local headgroup environment. As a hydrophobic molecule, C_{60} would be expected to possess greater stability in the alkyl tail group region of the bilayer, which is confirmed by inspection of the relative depth of the free-energy potential. The free-energy minimum of 76 $\pm$ 4 kJ/mol and 0.9 nm offset from the bilayer center in this study is comparable to reported values at 0.7 nm, 0.9 nm, 1.0 nm, and 1.1 nm with corresponding depths of 84 kJ/mol, 100 kJ/mol, 110 kJ/mol, and 35 kJ/mol in neat DMPC (26), dipalmitoylphosphatidylcholine (DPPC) (44), and dioleoyl phosphatidylcholine (DOPC) (44), and DPPC (43), bilayers,

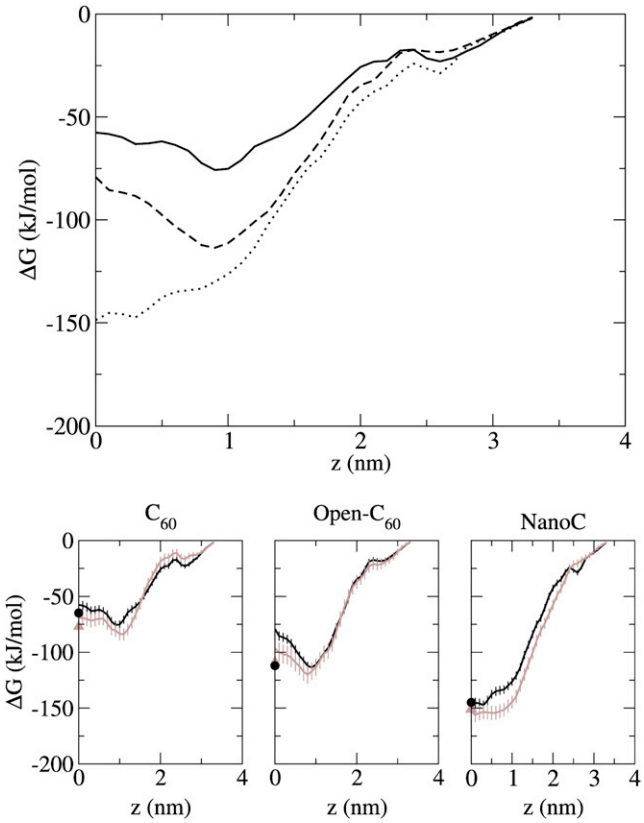


FIGURE 2 (*Top*) Free-energy profile of C_{60} (*solid line*), Open-C_{60} (*dashed line*), and NanoC (*dotted line*) along the DMPC/cholesterol bilayer norm. (*Bottom*) Semiisotropic (*black line*) and isotropic (*gray line*) barostat scaling. TI values (*black circle*) are displayed at the abscissa origin.

respectively. Although the geometrical offset from the bilayer center has been rationalized by enthalpic calculations (26,43), a rigorous thermodynamic decomposition of the free energy in this region would be desirable. Because a reasonable agreement is obtained between the TI (65 kJ/mol) and CF values (58 ± 4 kJ/mol) at the bilayer center in this study, we attribute the discrepancies in free-energy depths and offset positions with respect to the aforementioned studies to differences in bilayer composition, simulation temperatures, and force-field parameterization. Similar free-energy profiles were obtained with isotropic and semiisotropic barostat coupling (Fig. 2), with the latter defined as expansion in the *xy*-plane decoupled that along the *z*-coordinate axis. This can provide an indirect indication of simulation convergence insofar as the lateral bilayer expansion with permeant embedment is adequately accommodated by the isotropic pressure coupling.

The free-energy profile of the combustion-generated particle, NanoC, differs in many respects from C_{60} (Fig. 2); however, there are similarities at the membrane interface. The absence of a permeation barrier from the aqueous phase into the headgroup region, and the similar free-energy slope indicate a predicted timescale of particle uptake comparable to that of C_{60}. Despite possessing a different structure and slightly larger particle size, NanoC generated a similar free-energy plateau in the headgroup region. In the bilayer alkane core, however, the calculated free-energy minimum of NanoC differed in position from C_{60} and was found to possess significantly greater binding. In fact, the binding energy of 143 ± 5 kJ/mol at the bilayer center is, to our knowledge, the highest reported for any nonbiological permeant in a lipid membrane to date. Additional confidence in this value was supplied by a TI ΔG value of 145 kJ/mol, which falls within the uncertainty of the CF calculation.

Differences in the interaction energetics of C_{60} and NanoC may be attributable to the different sizes and/or morphologies of the two molecules. To determine the sensitivity of the permeation process due solely to differences in particle structure, we considered a structural isomer of C_{60} in a form similar to NanoC. To match the general hemispherical shape of NanoC and maintain the pentagonal and hexagonal faces of C_{60}, we designed a prototypical opened buckyball structure, designated here as Open-C_{60}, by paring a larger fullerene (C_{100}) to a 60-carbon atom structure (Fig. 1). For direct comparison to C_{60}, the exposed rim atoms on Open-C_{60} were assigned resonant carbon nonbonding interaction parameters. In the headgroup region, the calculated Open-C_{60} free-energy values (Fig. 2) display the plateau form, consistent with the profiles of the similarly sized C_{60} and NanoC permeants. The discrepancy in binding energies becomes particularly prominent in the membrane core, although even in the headgroup region the Open-C_{60} free-energy values rival those of the deeper-bound NanoC. Notably, the calculated Open-C_{60} free-energy binding exceeds that of its C_{60} counterpart in all regions of the membrane interior. The Open-C_{60} free-energy minimum is offset from the bilayer center by 0.9 nm, which matches the offset of C_{60}. A relatively low barrier also appears in the bilayer center; however, the value and confidence cannot be assigned to the height due to moderate variability of the CF and TI free-energy calculations. Use of the semiisotropic and isotropic barostats yielded CF binding depths of 97 kJ/mol and 79 kJ/mol, respectively, whereas TI depth values were calculated to be 109 kJ/mol and 112 kJ/mol, respectively.

We note that the binding free energies of the three nanometer-sized carbonaceous permeants significantly exceed literature values for carbonaceous small molecules, including benzene (20 kJ/mol (19)), hexane (24 kJ/mol (15)), and ethane (23 kJ/mol (19)). The particle size differences thus increase the negative ΔG of permeation by either attenuating the enthalpic differences or accentuating the entropic differences of permeants embedded in the bilayer with respect to the aqueous phase. A comparison of the free-energy profile differences between C_{60} and Open-C_{60}, however, allows us to remove from consideration an effect based solely on the molecular mass, i.e., the atom number. In this instance, the sizable free-energy differences are based solely on the permeant morphology.

Orientation

Assessment of the variability of particle orientation in the bilayer can lend insight into the entropic contribution of the permeation process. A recent MD study, however, demonstrated that the permeation process can include competitive enthalpy and entropy contributions (15). The negative free-energy difference for hexane partitioning from the water layer into the phosphatidylcholine headgroup region of a DOPC membrane was determined to have an enthalpic origin. This contrasted with the entropically driven propagation of the molecule in the bilayer interior. The ubiquity of enthalpically driven portions of the permeation processes remains undetermined, and Xiang and Anderson (6) asserted that this nonclassical hydrophobic effect may drive the initial permeation for a ''large number of molecules''.

The entropic differences that result from the permeant transferring from the water to a lipid environment balance the gains and losses in the order of the permeant molecule and that of the surrounding environment. In this study, we can extract an indication of one of these terms: the rotational ordering imposed by the water and lipid environments as reflected by the permeant alignment. An indication of restricted permeant motion is given by the propensity for anisotropic permeant molecules to align parallel to the bilayer norm (12,47,48). In this study, we monitored permeant orientation by analyzing the permeant principal axes of inertia, as described in Materials and Methods (Fig. 3). As shown in Fig. 4, the spherical C_{60} molecule possessed a random orientation, as evidenced by the high variance of the mean orientation angle ($\langle\theta\rangle$) and the averaged value of alignment of the permeant face, between 0° (perpendicular to bilayer norm) and 90° (parallel). Note that similar values were obtained for Open-C_{60} and NanoC at positions in the water layer. Of interest, the latter two particles became more aligned within the tail group region ($z < 1.4$ nm), as evidenced by the low mean orientation values and variation profiles that clearly display attenuated permeant oscillations. Based on this evaluation, we conclude that the aspherical nanoparticles considered in this study are more ordered within the bilayer interior, which is consistent with previous determinations for small molecules (12). We can also indirectly assess the entropic implications that the permeants impose on the local bilayer environment by evaluating the lateral diffusion constant values of lipid molecules in the presence of similarly sized permeant molecules (5). It is apparent that the particles attenuate local lipid translational motion, which also decreases system entropy. A complete determination of the change of entropy in the diffusion process would also require consideration of the thermodynamics of the permeant in the water layer. Size-based studies of prototypical solutes (16,17) predicted that the insertion of large solutes, defined as twice the size of a water molecule, will generate a minimal entropic change. This was rationalized by the fact that the water molecules in the first shell of a large solute would be geometrically limited in the alignment of hydrogen bonds. As such, for the nanoparticles considered in this study, the fact that the morphologic-based, free-energy binding depths (Fig. 2) scale inversely to the permeant ordering in the bilayer interior may indicate a relatively minor entropic contribution to the overall free energy in that region.

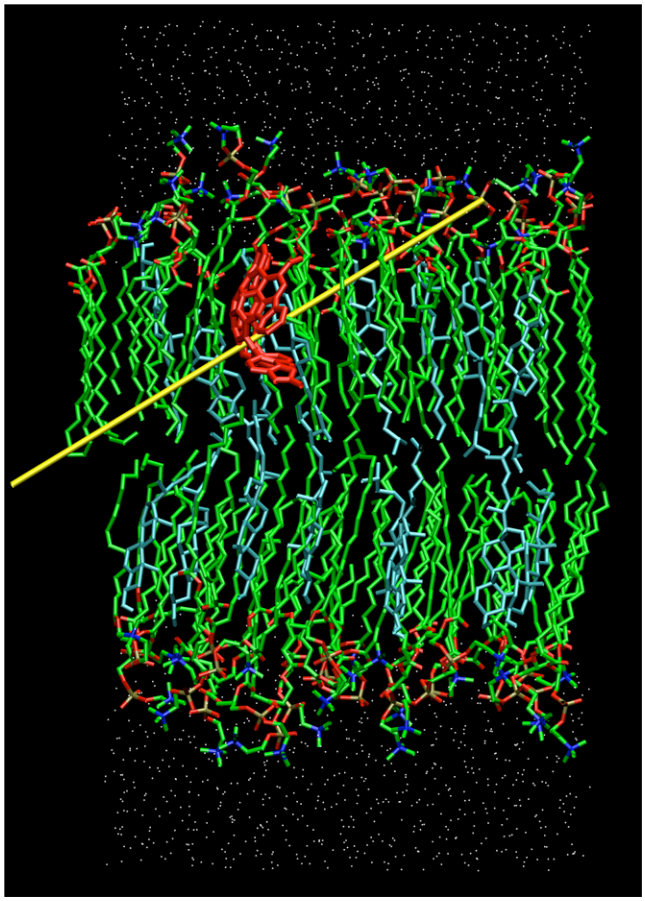


FIGURE 3 Permeant (NanoC) orientation reflected by the principal axis corresponding to the largest moment of inertia. The angle is defined as zero with the molecular major axis perfectly aligned parallel to the bilayer norm, i.e., a horizontal principal axis.

Diffusion

Diffusion constant profiles were calculated for C_{60}, Open-C_{60}, and NanoC molecules (see Fig. 6) by employing the force autocorrelation approach (Eq. 1) discussed above. Due to the relatively large noise associated with FAC calculations, greater statistics were acquired by averaging multiple trajectories (7–10) at five positions along the bilayer norm. The positions were selected to span defined regions of the bilayer environment (35,45,46)—the bilayer center, tail group region, headgroup region, interface, and water layer—at $z = 0.0$, 0.9, 1.7, 2.5, and 3.3 nm, respectively. Thus, multiple FAC plots were averaged at each position, fit to

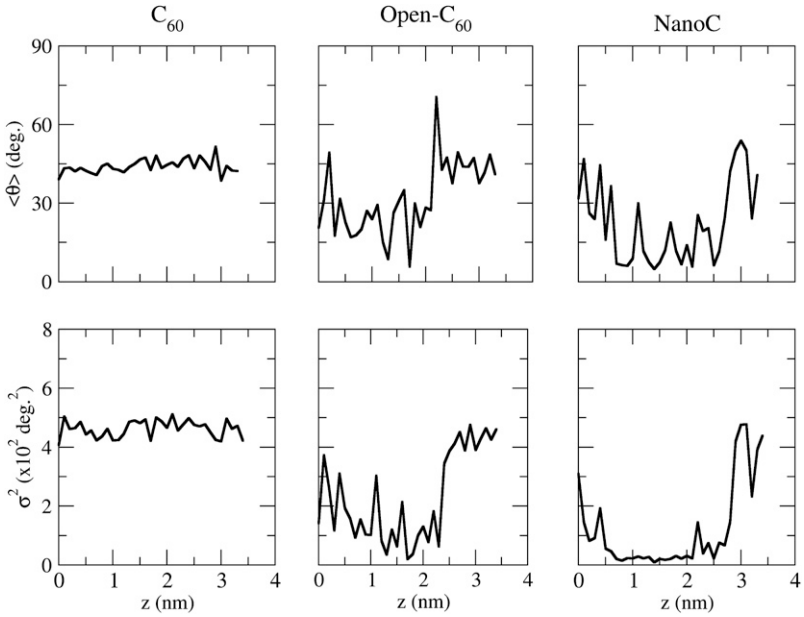


FIGURE 4 (*Top*) Average orientation of the permeant molecules as defined in Fig. 3. (*Bottom*) Square of the orientation variance.

a double exponential decay, and integrated (e.g., Fig. 5). A standard error approximation was calculated by first fitting the individual FAC calculations to yield a set of diffusion constant values at each position. As a point of reference, the C_{60} diffusion constant values can be compared to the literature values. Values in the interior region ($z < 2.5$ nm) appear to match the general linearity and range (10^{-8}–10^{-7} cm^2/s) calculated in a DMPC bilayer (26), and values in both studies appear slightly attenuated as compared to a coarse-grained C_{60} permeating a DOPC bilayer (44). This may be attributed to the fact that coarse-graining is known to accelerate the dynamics (on the simulation timescale), as evidenced by higher lateral diffusion constant values of coarse-grained lipid systems (49). The diffusion constant value (1.6×10^{-6} cm^2/s) in the water phase ($z = 3.3$ nm) remains attenuated with respect to the DOPC study (~3×10^{-6} cm^2/s) (44) and, to a greater extent, the DMPC study (~7×10^{-6} cm^2/s) (26). We note, however, that the latter study employed carbon-water oxygen potentials with a smaller CO binding depth ($\varepsilon = 0.39$ kJ/mol) than generated by the OPLS potentials used in our study ($\varepsilon = 0.50$ kJ/mol). It is probable, then, that this parameterization is also the origin of the discrepancy between experimental diffusion constant values (0.83–2.4 $\times$ 10^5 cm^2/s) and simulations in neat water (0.82–1.27 $\times$ 10^{-5} cm^2/s) (50). Although better agreement could be obtained with alternative C_{60}/H_2O potential parameters, we retained the OPLS parameters in this study for consistency, and because permeability in the bilayer interior should remain largely unaffected by permeant/solvent interactions.

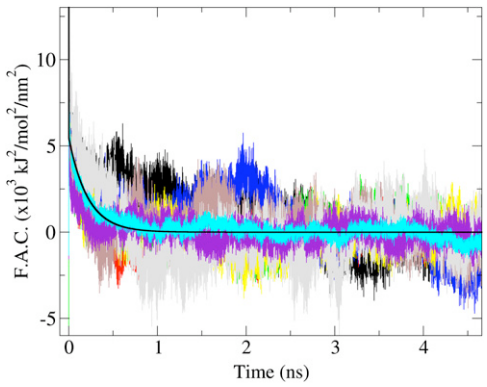


FIGURE 5 Force autocorrelation function of eight NanoC trajectories at $z = 0$ nm. The averaged FAC value (*cyan*) was fit (*black line*) to a double exponential decay with decay constants of 0.004 ps and 14 ps. (For interpretation of the reference to color in this figure legend, the reader is referred to the online version of this article.)

The diffusion constant profiles obtained for Open-C_{60} and NanoC also possess relatively constant values in the bilayer interior. The lack of sensitivity of diffusion to solute size in the bilayer interior as compared to the solute in water was previously noted (12), and relatively constant values that were independent of permeant position in the membrane were previously reported for a nifedipine drug analog, $C_{18}NO_4H_{20}$ (6,51).

Resistance and permeability

Equation 2 was applied to calculate the local resistance profiles (Fig. 6). Similar resistance values were obtained for the three nanopermeants in the water layer, and comparable values were previously calculated by Bedrov et al. (26) for C_{60}. Relatively minor barriers of resistance are displayed by the profiles, supporting the notion of spontaneous insertion (26). Progressively attenuated resistance values are apparent in the membrane core region ($R_{C60} \gg R_{Open\text{-}C60} \gg R_{NanoC}$), due in large part to the exponential dependence (Eq. 2) on the free-energy values (Fig. 2).

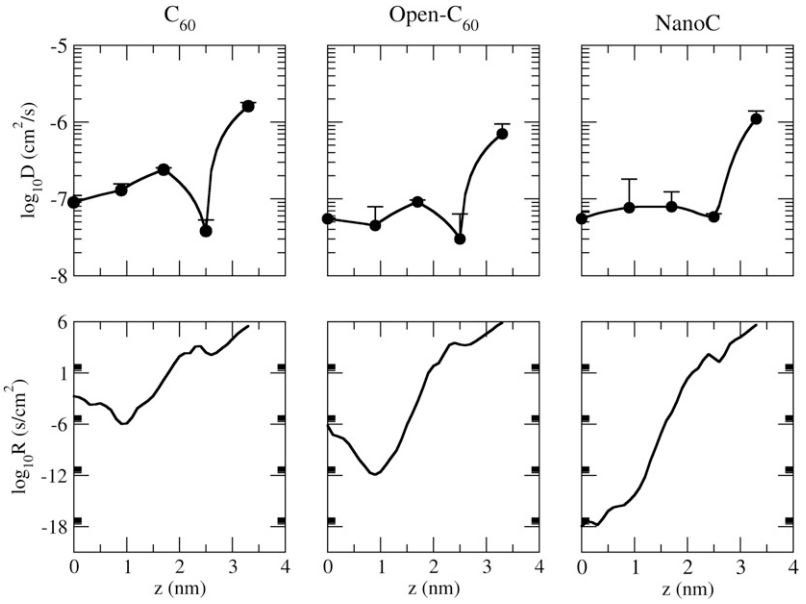


FIGURE 6 Diffusion (*top*) and resistance constant profiles as calculated by autocorrelation of the instantaneous force (Eq. 1) and the solubility-diffusion approach (Eq. 2), respectively.

Since the resistance for the permeants considered in this study is not negligible in the water layer, calculation of the permeability coefficient (Eq. 2) requires an assessment with regard to the local resistance integration limits, i.e., the bilayer thickness (52). The location of the bilayer interface, however, is not discrete, and an excessively liberal estimate of the monolayer thickness (defined in this discussion as z') could distort the calculated value of the partition coefficient, since the permeant in the water layer yields $\Delta G(z > \text{interface}) \rightarrow 0$ and $D(z > \text{interface}) \rightarrow D_{aq}$, the aqueous diffusion constant of the permeant. Substituting these values into Eq. 3 ultimately improperly decreases the value of the permeability coefficient by addition of a second term, c, in the denominator:

$$P = \frac{1}{\int_{z'}^{0} R(z)dz} = \frac{1}{\int_{\text{interface}}^{0} \frac{\exp(\Delta G(z)/RT)}{D(z)}dz + c} \quad (7)$$

where $c = \Delta z/D_{aq}$, with Δz as the distance difference of z' to the interface. Integrating well into the water bilayer ($z =$ 3.3 nm) yields calculated permeability coefficients of C_{60}, Open-C_{60}, and NanoC as 330 cm/s, 120 cm/s, and 250 cm/s, respectively. As expected, the permeability coefficient values increase when consideration is limited to the bilayer interior. For example, setting the upper integration limit to $z = 2.5$ nm, i.e., the diffusion constant break point shown in Fig. 6, yields calculated permeability coefficients of C_{60}, Open-C_{60}, and NanoC as 2.8×10^4 cm/s, 1.5×10^4 cm/s, and 3.9×10^5 cm/s, respectively. This illustrates the sensitivity of the permeability coefficient values of the nanometer-sized permeants to the integration limits in Eq. 3, and demonstrates a limitation of the inhomogeneous solubility diffusion model for this class of hydrophobic molecules. As such, in this study only intramembrane NP diffusion was considered to fall within an acceptable window of validity. Nevertheless, the attenuation of the permeability coefficient values by two to three orders of magnitude, based on the slightly larger integration limit, indicates that the adjacent unstirred aqueous layer may significantly contribute as a barrier to the permeation process. This would, in turn, influence the calculated value of the permeability coefficients; however, interrogation of this effect is beyond the scope of this study. Nevertheless, it is apparent that the relatively large permeability coefficient values within the membrane denote a high lipophilicity of these carbonaceous particles. Although individual hydrophobic particles in this class are known to aggregate in water, computational simulations have indicated a dissolution mechanism upon penetration of the membrane (44). Larger, $PM_{2.5}$ carbonaceous nanoparticles (<2.5 nm) have been shown to be capable of serving as a transport scaffold for small organic aromatic hydrocarbons, which can selectively absorb into the cell membrane (53). Therefore, it is not implausible to also consider composite particles depositing loosely bound nanoparticles, in essence establishing an alternative mechanism of transporting the hydrophobic nanoparticles through aqueous regions. Thus, factors governing the permeation of C_{60}-sized carbonaceous nanoparticles may ultimately influence ultrafine particle toxicity.

CONCLUSIONS

MD simulations were employed to interrogate the passive permeation process of three similarly sized nanoparticles—a representative combustion-generated nanoparticle, C_{60}, and a prototypical half buckyball-shaped molecule also composed of 60 carbon atoms—through a representative

cell membrane. Free-energy profiles were calculated along the bilayer norm with the CF approach and validated with a single point TI calculation at the bilayer center. Good agreement was obtained between the two methods, as well as in a profile comparison of C_{60} with a recent MD simulation reported in the literature. It was shown that the nano-sized permeants possessed larger binding values than smaller carbonaceous molecules, and that significant variability of the binding depths existed with respect to the nanopermeant morphology. The orientation of the anisotropic nanoparticles was ascertained by monitoring the angle of the appropriate principal axis of inertia. The orientations of the anisotropic nanoparticles were constrained in the bilayer interior, as was previously observed for smaller-sized permeants. The diffusion, resistance, and permeability coefficients of the nanopermeants were assessed as part of the inhomogeneous solubility-diffusion approach. In accordance with the literature, relatively little variation of the diffusion constant was found in the bilayer interior as compared to that of smaller permeants. The resistance constant profile varied greatly with nanoparticle morphology, which was predominantly attributed to the exponential dependence of the corresponding free-energy values. Significant variance and sensitivity of the permeability coefficient was observed, based on particle morphology and assessment of the bilayer width. Given the drastic differences in thermodynamic and permeation values, this study indicates that C_{60} may not adequately represent a class of similarly sized but morphologically different combustion-generated nanoparticles with regard to assessments of nanotoxicity.

The authors thank Mr. Nicholas Burtch and Mr. Alexander Itkin for assistance with data collection, analysis, and figure preparation.

This work was funded by a National Science Foundation grant (CBET 0644639). Research was supported in part by the National Science Foundation through TeraGrid resources.

REFERENCES

1. Nel, A., T. Xia, …, N. Li. 2006. Toxic potential of materials at the nanolevel. *Science*. 311:622–627.
2. Bothun, G. D. 2008. Hydrophobic silver nanoparticles trapped in lipid bilayers: size distribution, bilayer phase behavior, and optical properties. *J. Nanobiotechnol.* 6:13.
3. Choe, S., R. Chang, …, A. Violi. 2008. Molecular dynamics simulation study of a pulmonary surfactant film interacting with a carbonaceous nanoparticle. *Biophys. J.* 95:4102–4114.
4. Xiang, T. X., and B. D. Anderson. 1998. Influence of chain ordering on the selectivity of dipalmitoylphosphatidylcholine bilayer membranes for permeant size and shape. *Biophys. J.* 75:2658–2671.
5. Chang, R., and A. Violi. 2006. Insights into the effect of combustion-generated carbon nanoparticles on biological membranes: a computer simulation study. *J. Phys. Chem. B*. 110:5073–5083.
6. Xiang, T. X., and B. D. Anderson. 2006. Liposomal drug transport: a molecular perspective from molecular dynamics simulations in lipid bilayers. *Adv. Drug Deliv. Rev.* 58:1357–1378.
7. Jacobs, R. E., and S. H. White. 1984. Behavior of hexane dissolved in dioleoylphosphatidylcholine bilayers—an NMR and calorimetric study. *J. Am. Chem. Soc.* 106:6909–6912.
8. Mulders, F., H. Vanlangen, …, Y. K. Levine. 1986. The static and dynamic behavior of fluorescent-probe molecules in lipid bilayers. *Biochim. Biophys. Acta*. 859:209–218.
9. Adler, M., and T. R. Tritton. 1988. Fluorescence depolarization measurements on oriented membranes. *Biophys. J.* 53:989–1005.
10. McIntosh, T. J., S. A. Simon, and R. C. MacDonald. 1980. The organization of n-alkanes in lipid bilayers. *Biochim. Biophys. Acta*. 597: 445–463.
11. Salafsky, J. S., and K. B. Eisenthal. 2000. Second harmonic spectroscopy: detection and orientation of molecules at a biomembrane interface. *Chem. Phys. Lett.* 319:435–439.
12. Bemporad, D., C. Luttmann, and J. W. Essex. 2005. Behaviour of small solutes and large drugs in a lipid bilayer from computer simulations. *Biochim. Biophys. Acta*. 1718:1–21.
13. Cohen, M. H., and D. Turnbull. 1959. Molecular transport in liquids and glasses. *J. Chem. Phys.* 31:1164–1169.
14. Mukhopadhyay, P., H. J. Vogel, and D. P. Tieleman. 2004. Distribution of pentachlorophenol in phospholipid bilayers: a molecular dynamics study. *Biophys. J.* 86:337–345.
15. MacCallum, J. L., and D. P. Tieleman. 2006. Computer simulation of the distribution of hexane in a lipid bilayer: spatially resolved free energy, entropy, and enthalpy profiles. *J. Am. Chem. Soc.* 128:125–130.
16. Southall, N. T., K. A. Dill, and A. D. J. Haymet. 2002. A view of the hydrophobic effect (vol 106, pg 523, 2002). *J. Phys. Chem. B*. 106: 521–533.
17. Southall, N. T., and K. A. Dill. 2000. The mechanism of hydrophobic solvation depends on solute radius. *J. Phys. Chem. B*. 104:1326–1331.
18. Trzesniak, D., A. P. E. Kunz, and W. F. van Gunsteren. 2007. A comparison of methods to compute the potential of mean force. *ChemPhysChem*. 8:162–169.
19. Bemporad, D., J. W. Essex, and C. Luttmann. 2004. Permeation of small molecules through a lipid bilayer: A computer simulation study. *J. Phys. Chem. B*. 108:4875–4884.
20. Marrink, S. J., and H. J. C. Berendsen. 1994. Simulation of water transport through a lipid-membrane. *J. Phys. Chem.* 98:4155–4168.
21. Vogelsang, R., and C. Hoheisel. 1987. Determination of the friction coefficient via the force autocorrelation function—a molecular-dynamics investigation for a dense Lennard-Jones Fluid. *J. Stat. Phys.* 47:193–207.
22. Roux, B., and M. Karplus. 1991. Ion-transport in a gramicidin-like channel—dynamics and mobility. *J. Phys. Chem.* 95:4856–4868.
23. Kubo, R. 1966. Fluctuation-dissipation theorem. *Rep. Prog. Phys.* 29:255–284.
24. Mamonov, A. B., M. G. Kurnikova, and R. D. Coalson. 2006. Diffusion constant of K^+ inside Gramicidin A: a comparative study of four computational methods. *Biophys. Chem.* 124:268–278.
25. Katz, R. J., P. S. Landau, …, C. Weise. 1993. Serotonergic (5-HT2) mediation of anxiety-therapeutic effects of serazepine in generalized anxiety disorder. *Biol. Psychiatry*. 34:41–44.
26. Bedrov, D., G. D. Smith, …, L. Li. 2008. Passive transport of C60 fullerenes through a lipid membrane: a molecular dynamics simulation study. *J. Phys. Chem. B*. 112:2078–2084.
27. Dennington II, R., T. Keith, …, R. Gilliland. 2003. GaussView, version 3.09. Semichem, Shawnee Mission, KS.
28. Violi, A. 2004. Modeling of soot particle inception in aromatic and aliphatic premixed flames. *Combust. Flame*. 139:279–287.
29. Violi, A., A. F. Sarofim, and G. A. Voth. 2004. Kinetic Monte Carlo molecular dynamics approach to model soot inception. *Combust. Sci. Technol.* 176:991–1005.
30. Violi, A., G. A. Voth, and A. F. Sarofim. 2005. The relative roles of acetylene and aromatic precursors during soot particle inception. *Proc. Combust. Inst.* 30:1343–1351.
31. Violi, A., and A. Venkatnathan. 2006. Combustion-generated nanoparticles produced in a benzene flame: a multiscale approach. *J. Chem. Phys.* 125:054302.

32. http://www.cochem2.tutkie.tut.ac.jp/Fuller/higherE.html. Accessed January 17, 2008.
33. Smith, W., and T. R. Forester. 1996. DL_POLY_2.0: a general-purpose parallel molecular dynamics simulation package. *J. Mol. Graph.* 14:136–141.
34. Violi, A., and R.W. Chang. 2006. Carbonaceous nanoparticles in lipid bilayers. *J. Am Chem. Soc.* Abstract. 231:105-FUEL.
35. Smondyrev, A. M., and M. L. Berkowitz. 1999. Structure of dipalmitoylphosphatidylcholine/cholesterol bilayer at low and high cholesterol concentrations: molecular dynamics simulation. *Biophys. J.* 77:2075–2089.
36. Smondyrev, A. M., and M. L. Berkowitz. 1999. United atom force field for phospholipid membranes: constant pressure molecular dynamics simulation of dipalmitoylphosphatidicholine/water system. *J. Comput. Chem.* 20:531–545.
37. Van Der Spoel, D., E. Lindahl, …, H. J. Berendsen. 2005. GROMACS: fast, flexible, and free. *J. Comput. Chem.* 26:1701–1718.
38. Berendsen, H. J. C., J. P. M. Postma, …, J. R. Haak. 1984. Molecular-dynamics with coupling to an external bath. *J. Chem. Phys.* 81: 3684–3690.
39. Parrinello, M., and A. Rahman. 1981. Polymorphic transitions in single crystals—a new molecular-dynamics method. *J. Appl. Phys.* 52:7182–7190.
40. Swope, W. C., H. C. Andersen, …, K. R. Wilson. 1982. A computer-simulation method for the calculation of equilibrium constants for the formation of physical clusters of molecules—application to small water clusters. *J. Chem. Phys.* 76:637–649.
41. http://plasma-gate.weizmann.ac.il/Grace/. Accessed July 25, 2006.
42. Bernath, P. F. 1995. Spectra of Atoms and Molecules. Oxford University Press, New York.
43. Qiao, R., A. P. Roberts, …, P. C. Ke. 2007. Translocation of C60 and its derivatives across a lipid bilayer. *Nano Lett.* 7:614–619.
44. Wong-Ekkabut, J., S. Baoukina, …, L. Monticelli. 2008. Computer simulation study of fullerene translocation through lipid membranes. *Nat. Nanotechnol.* 3:363–368.
45. Davis, J. E., O. Rahaman, and S. Patel. 2009. Molecular dynamics simulations of a DMPC bilayer using nonadditive interaction models. *Biophys. J.* 96:385–402.
46. Kucerka, N., Y. F. Liu, …, J. F. Nagle. 2005. Structure of fully hydrated fluid phase DMPC and DLPC lipid bilayers using X-ray scattering from oriented multilamellar arrays and from unilamellar vesicles. *Biophys. J.* 88:2626–2637.
47. Hoff, B., E. Strandberg, …, C. Posten. 2005. 2H-NMR study and molecular dynamics simulation of the location, alignment, and mobility of pyrene in POPC bilayers. *Biophys. J.* 88:1818–1827.
48. Xiang, T. X., and B. D. Anderson. 1994. Molecular distributions in interphases: statistical mechanical theory combined with molecular dynamics simulation of a model lipid bilayer. *Biophys. J.* 66:561–572.
49. Izvekov, S., and G. A. Voth. 2006. Multiscale coarse-graining of mixed phospholipid/cholesterol bilayers. *J. Chem. Theory Comput.* 2:637–648.
50. Maciel, C., E. E. Fileti, and R. Rivelino. 2009. Note on the free energy of transfer of fullerene C60 simulated by using classical potentials. *J. Phys. Chem. B.* 113:7045–7048.
51. Alper, H. E., and T. R. Stouch. 1995. Orientation and diffusion of a drug analog in biomembranes—molecular-dynamics simulations. *J. Phys. Chem.* 99:5724–5731.
52. Marrink, S. J., and H. J. C. Berendsen. 1996. Permeation process of small molecules across lipid membranes studied by molecular dynamics simulations. *J. Phys. Chem.* 100:16729–16738.
53. Penn, A., G. Murphy, …, L. Penn. 2005. Combustion-derived ultrafine particles transport organic toxicants to target respiratory cells. *Environ. Health Perspect.* 113:956–963.